A NEW CURVATURE MORPHING SKIN: MANUFACTURING, EXPERIMENTAL AND NUMERICAL INVESTIGATIONS

A. Schmitz*[1], P. Horst[1]

[1] *Institute of Aircraft Design and Lightweight Structures, TU Carolo-Wilhelmina Braunschweig, Hermann-Blenk-Strasse 35, 38108 Braunschweig, Germany.*
* *Corresponding Author: a.schmitz@tu-braunschweig.de*

Keywords: Curvature morphing skin, Homogenisation, Large bending experiment, Hybrid composite

Abstract
Currently, the aerospace sector tries to bring morphing technology into application in order to improve flight performance, reduce noise and extend the operational envelope. This work presents a new curvature morphing skin which is intended to be applicable at a highly contour-variable airliner's droop nose. The key characteristic of such skin is a large curvature at rupture in droop-direction while simultaneously providing a high perpendicular stiffness. Hence, two manufacturing processes for a hybrid composite-elastomer skin have been developed. After introducing the structural concept with the appropriate manufacturing processes, large bending experiments are presented. Finally, in order to gain further understanding, some numerical investigations are performed by using a finite element unit-cell.

1. Introduction

Adopting structures in order to gain optimal performance in the actual prevailing condition has always been a topic within the aerospace sector. A comprehensive review on morphing applications is given by Barbarino et al. [1].
This work focusses on a skin structure for curvature morphing applications which exceeds the possibilities of standard materials. Particularly, it could serve as skin for a contour-variable droop-nose recently investigated by Burnazzi and Radespiel [2] with a 90° droop of the stagnation point. In comparison, the contour-variable GFRP droop nose investigated within the European project SADE [3] with about 25° droop of the stagnation point and 1 mm minimum skin thickness constitutes the curvature morphing limit of GFRP. A slight overview of the curvature morphing potentials of some standard aerospace materials is given in [4].
Similar to other morphing structures (e.g. for changing area) also curvature morphing skins must show the contradictory characteristic of having a high deformation until rupture and also a sufficient rigidity to carry external loads. Typically, this key requirement is treated by imposing an extreme anisotropy. However, in contrast to area morphing, curvature morphing skins mostly need to feature a frequent change of their (bending) stiffness properties along the morphed contour [3]. The presented skin exhibits a layered structure, see Fig. 1, and can thus be manufactured with standard composite tooling, which is a strong benefit compared to other candidates like e.g. corrugated composites [5]. The structural concept sketched in Fig. 1 involves

a centred FRP laminate and discrete, compliantly embedded stiffeners. Presuming a reasonable connection between all structural parts (stiffeners, FRP laminate and compliant matrix) the compliant matrix takes the high bending normal strain in morphing-direction, while the continuous stiffeners provide a high transverse (bending) stiffness. Note, that the direct combination of technical fibres with a compliant matrix (known as chord-rubber composites) leads to a very low bending and compression strengths due to the poor buckling support of the rubber-like matrix.

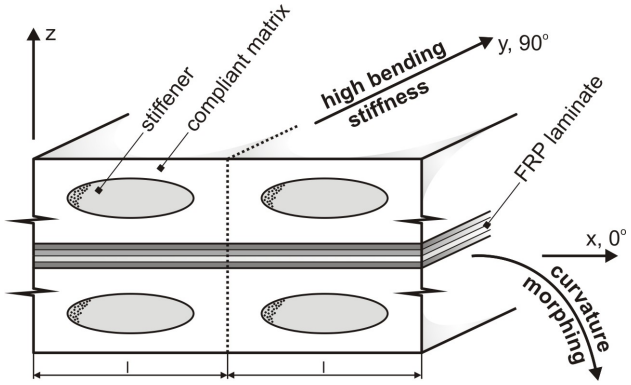

Figure 1. Sketch of the structural concept of the curvature morphing skin.

The subsequent work is structured as follows. Firstly, the manufacturing process is described and important properties of the constituent materials are given. Then, static bending experiments are presented. Finally, a finite element unit-cell of the manufactured structure is introduced, validated and used for further insights.

2. Materials and manufacturing

The suggested structural concept has been realised by two completely different manufacturing processes and constituent materials. One process results in opaque samples whereas the other is characterised by improved performance and manufacturability. Due to the possibility of visual inspection of the opaque samples via transmitted light scanning, the following experimental investigations deal with these samples. So far, all samples consist of centred 0° (fibres oriented in morphing-direction) FRP laminate and symmetrically assembled, transverse 90° stiffeners.

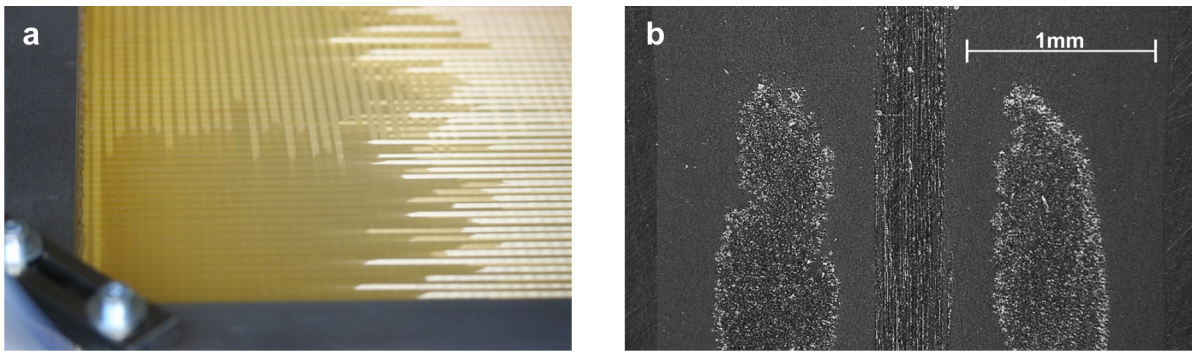

Figure 2. Second manufacturing step of the opaque samples (a) and a corresponding polished section (b).

The opaque samples are manufactured in a two-stage process. Firstly, E-glass-fibre rovings OC-111A (1200 tex) are CNC-placed and stacked with thermoplastic polyurethane elastomer (TPU) films. Afterwards the elastomer is melt around the glass rovings under vacuum. Note, that after this step the glass rovings are only enclosed by the TPU and not impregnated. In a second step the rovings are impregnated with epoxy resin/hardener Momentive RIM135/RIMH137, see Fig. 2(a). Except the fact that each roving has its own mould of surrounding TPU, this step is a resin transfer moulding (RTM) process with about 2 bar pressure and −0.9 bar vacuum. A polished section of the resulting structure is given in Fig. 2(b). From these the geometry is measured with a digital microscope for subsequent numerical modelling.

E_m	3400	MPa	ν_m	0.38	–	$V_\mathrm{f,FRP}$	57	%
E_f	80700	MPa	ν_f	0.22	–	$V_\mathrm{f,sti}$	67	%
E_TPU	29.2	MPa	ν_TPU	0.46	–	$R^+_{\perp,\mathrm{sti}}$	40	MPa

Table 1. Material data of the opaque TPU hybrid samples.

E_m	3390	MPa	ν_m	0.38	–	$V_\mathrm{f,FRP}$	68	%
E_f	68584	MPa	ν_f	0.25	–	$V_\mathrm{f,sti}$	68	%
E_EPDM	7.7	MPa	ν_EPDM	0.45	–	$R^+_{\perp,\mathrm{sti}}$	83	MPa

Table 2. Material data of the EPDM hybrid samples.

The structure obtained by the second process is used for perspective numerical investigations. These samples are manufactured in a hand lay-up process of E-glass fibre prepreg and thermoset EPDM rubber. Important material data of the constituents is given for the opaque TPU (Tab. 1) and the EPDM hybrid samples (Tab. 2). Herein, the subscript $\bullet_\mathrm{m}$ indicates an epoxy resin and $\bullet_\mathrm{f}$ a glass fibre property.

3. Bending experiments

The suggested skin is intended for curvature morphing applications. Thus, first experimental investigations deal with measurements of bending moduli and the morphing curvature at rupture. These data is compared to numerical results in Section 4.

3.1. Measurement of the morphing and transverse bending moduli

All initial bending stiffness measurements have been conducted on a bending machine with a 1000 N load-cell and inductive as well as laser triangulation displacement recording. The opaque samples show a mean total thickness of $t = 2.495$ mm, a repeated unit-cell length (c.p. Fig. 1) of $l = 4.49$ mm, a stiffener cross section of $A = 1.33$ mm^2 and a centred FRP laminate thickness of $t_\mathrm{FRP} = 0.37$ mm. It has been demonstrated, that the variation of the outer support length in 3 and 4-point bending experiments did not considerably effect the resulting (morphing) bending modulus $E_x = 355 \pm 12$ MPa ($n = 3$).
In contrast, due to the compliant TPU surface with respect to the relatively high transverse bending stiffness the transverse samples are indented by the bending supports. Hence, the force against indentation displacement has been recorded in separate tests and has been used to correct the transverse modulus measurements. Additionally, the ratio of bending to shear

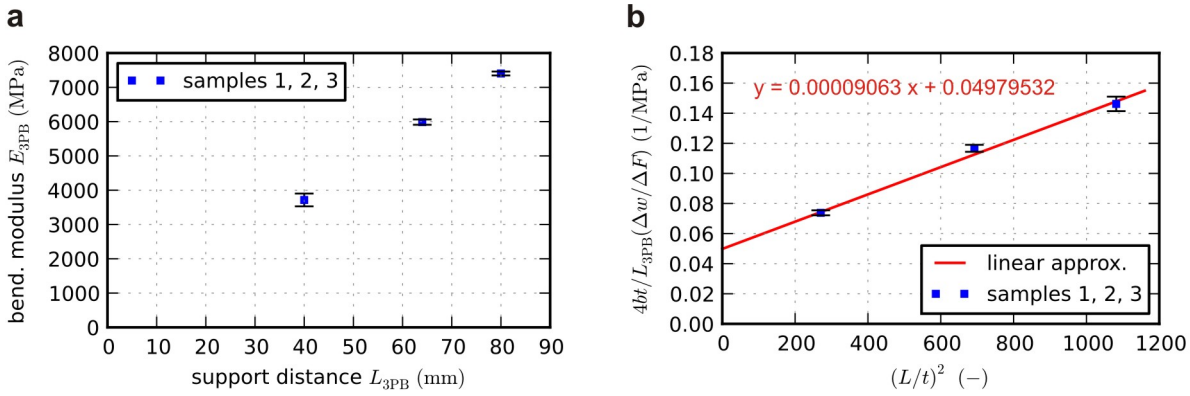

Figure 3. Initial transverse bending modulus via 3-point bending. (a) shows the modulus against outer support length and (b) the corresponding normalised illustration. The standard deviation bars apply for 3 samples.

stiffness turned out to be disadvantageous for standard (Bernoulli beam theory) measurement of the bending modulus E_y. Precisely, Fig. 3(a) illustrates the different results against outer support distance, hence available shear stress. However, in order to determine both, the pure transverse bending modulus E_y and the corresponding shear modulus G_y, the shear-compliant 3-point bending mid-deflection

$$w = \frac{FL^3}{4E_y bt^3} + \frac{kFL}{4G_y bt} \tag{1}$$

is rearranged following [6] as

$$\frac{4bt}{L}\frac{\Delta w}{\Delta F} = \frac{1}{E_y}\left(\frac{L}{t}\right)^2 + \frac{k}{G_y}\,. \tag{2}$$

Herein, b denotes the sample width, F the 3-point bending force, L the outer support distance and k the shear correction factor which is commonly chosen as $k = 1.2$ in such case. Figure 3(b) shows the experimental results and the corresponding linear approximation via eq. (2). With this correlation the transverse modulus is determined to $E_y = 11034$ MPa and $G_y = 24.1$ MPa.

3.2. Large bending degradation

After having recorded the initial bending moduli, the damage topology due to curvature morphing is investigated next. For this reason, the samples are subjected to an almost constant

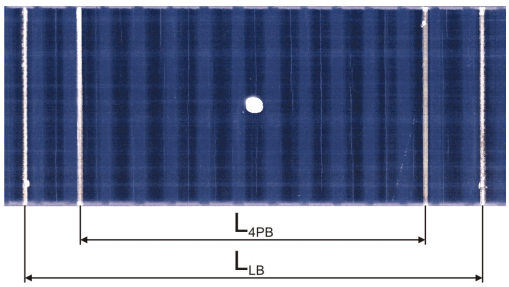

Figure 4. Transmitted light scan of a hybrid TPU sample which had been subjected to 34.5 1/m curvature.

curvature using a constructed large bending device, see Fig. 5(a) and [4, 5] for details regarding

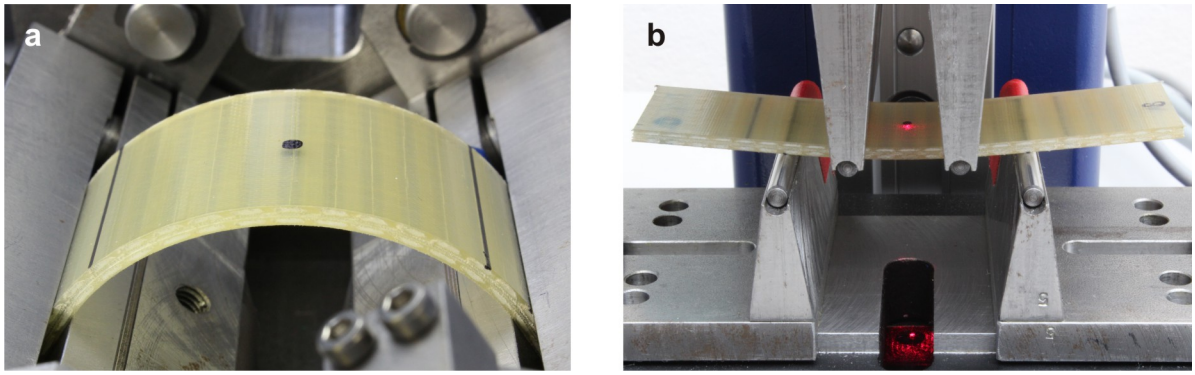

Figure 5. Hybrid TPU sample subjected to 34.5 1/m curvature in the large bending device (a) and measurement of the initial morphing bending modulus via 4-point bending (b).

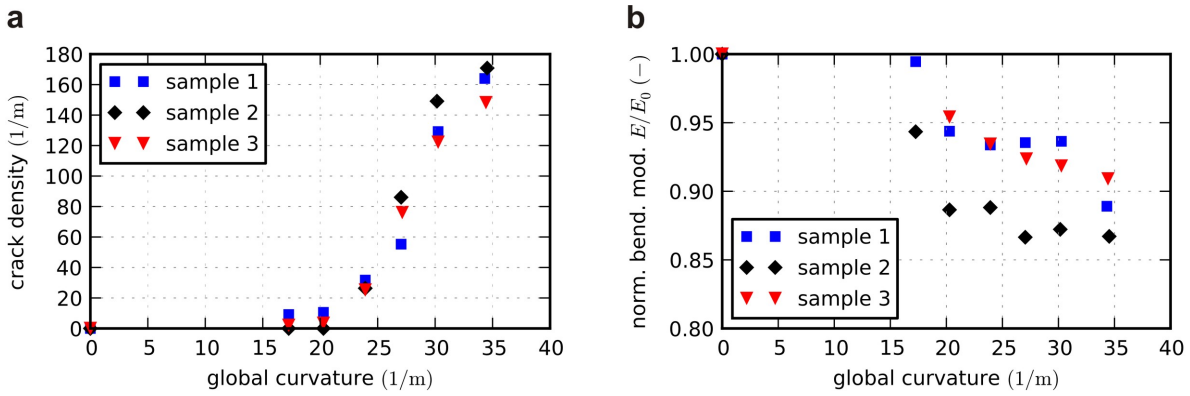

Figure 6. Transverse crack density (a) and normalised bending stiffness degradation (b) against global large bending curvature.

this fixture. The reduction of stiffness has been chosen as first common degradation indicator. Hence, the samples are subjected to a stepwise increasing large bending curvature with bent sample length $L_{\mathrm{LB}} = 59$ mm. For each step the initial bending stiffness is recorded via 4-point bending, see Fig. 5(b), with outer support distance $L_{\mathrm{4PB}} = 45$ mm and inner support distance $L' = 20$ mm. Additionally, a transmitted light scan is always conducted, see Fig. 4. Due to the fact that the GFRP stiffener material alone is completely transparent, the transverse stiffeners appear dark in the scans. It can be stated, that transverse cracks within the 90° glass-fibre/epoxy stiffeners at the bending tension side constitute the single visible damage. Hence, delaminations and failure between the elastomer-stiffener interface are not observed. In order to characterise the static evolution of transverse cracks and the corresponding bending stiffness degradation, the crack-density is evaluated for the 4-point bending section. Thus, the crack-density $\rho = n/L_{\mathrm{4PB}}$ is defined as the number of cracks n within sample sector L_{4PB} (c.p. Fig. 4). Herein, the number of cracks is normalised with the sample width w as

$$n = \frac{1}{w} \sum_{i}^{N} l_i \,. \tag{3}$$

Note, that this is generally an odd number. The length of the ith crack is denoted by l_i and the even number of available (also partial) cracks by N. Figure 6(a) shows the measured crack-density against global curvature. In spite of the hybrid structure, the S-type course of the

transverse cracking behaviour is similar to standard GFRP. The corresponding bending stiffness degradation is illustrated in Fig. 6(b). In contrast to standard cross-ply $[90, 0]_s$ GFRP, transverse cracks inside the stiffeners affect the bending stiffness less. However, note the measured degradation is also influenced by changes of the elastomer like the Mullins-effect.

4. Numerical investigations

This section presents the implementation of a finite element unit-cell of the hybrid skin structure. After comparing the model with the conducted experiments, some key parameters are investigated.

4.1. Finite element unit-cell

The finite element unit-cell is implemented following [7, 8]. The important characteristic of this technique is the homogenisation in the sense of the 2D classical laminated plate theory at the scale of the whole laminate including all bending, twisting and inplane-bending coupling terms. Hence, heterogeneities which exceed ply-level homogenisation capabilities can be dealt with which is the case for this hybrid structure.
The structural principle of preventing the stiffeners from bending normal strain can be observed in Fig. 7. The model is set up using the geometry given in Section 2. Thereby, the stiffener geometry is modelled with respect to its measured length, hight and cross-section area as an ellipse with centred intersecting rectangle. A mesh convergence study has been done.

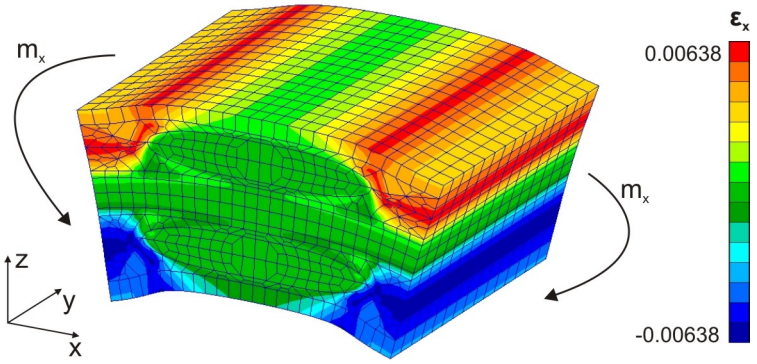

Figure 7. Representative finite element unit-cell of the manufactured hybrid TPU samples. The deformed (exaggerated) unit-cell is loaded by a pure moment flux. The coloured contours illustrate the normal bending strain.

With the unit-cell model at hand, the classical laminated plate theory stiffness matrix of the manufactured hybrid TPU samples is calculated as

$$\mathbf{ABD} = \begin{bmatrix} \mathbf{A} & \mathbf{B} \\ \mathbf{B} & \mathbf{D} \end{bmatrix} = \begin{bmatrix} 18210 & 1549 & & & & \\ & 38025 & & & & \\ & & 1571 & & & \\ & & & 457 & 94 & \\ & & & & 15346 & \\ & & & & & 111 \end{bmatrix} \quad (4)$$

with units [**A**] = N/mm, [**D**] = Nmm and [**B**] = N. At this point, the large ratio of transverse to morphing bending stiffness is obvious as well as the very small anticlastic bending deformation

behaviour. The bending moduli E_x and E_y are then calculated from the entries D_{11} and D_{22}, respectively, via

$$E_{x/y} = D_{11/22}\frac{12}{t^3}\,. \tag{5}$$

Hence, the moduli are well determined as $E_x = 353$ MPa (99.4 % of the experimental value) and $E_y = 11857$ MPa (107.5 % of the experimental value). Using a maximum stress failure criterion, the linear curvature at transverse rupture within the stiffeners is calculated as $\hat{\kappa}_x^{\mathrm{sti}} = 21.1\ \mathrm{m}^{-1}$, which is consistent with the experiment, cp. Fig. 6(a).

4.2. Perspective numerical analyses

With the finite element unit-cell at hand, some first analyses are performed. The hybrid structure is build with the EPDM elastomer and the material data given in Tab. 2. In order to investigate meaningful configurations all subsequent structures show transverse compression and tension failure of the centred 0° FRP laminate before failure of the stiffeners. In case of transverse compression, the stiffener's critical buckling stress has been analytically estimated so far. This way, the whole structure is always improved in transverse direction compared to the FRP laminate itself. In the following, the curvature at rupture

$$\hat{\kappa}_x^{\mathrm{sti}} = S_{\mathrm{min}}^{\mathrm{sti}}\,\kappa_x \tag{6}$$

is linearly extrapolated from linear finite element analyses by multiplication of the actual curvature κ_x with the corresponding minimum safety-factor within the stiffener obtained via a maximum stress failure criterion. Although this is a linear approximation, it is well suited for understanding the influence of some key parameters.

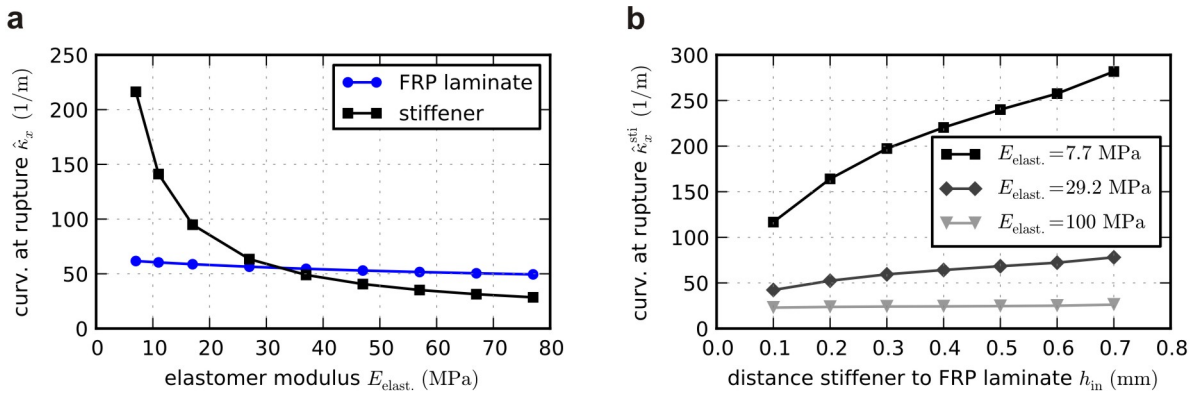

Figure 8. Investigation of the effect of the elastomer modulus $E_{\mathrm{elast.}}$ (a) and the distance between the FRP laminate and the stiffener h_{in} (b).

The investigated structure has a unit-cell length of $l = 4$ mm, a stiffener cross-section of $A = 1$ mm^2 and a FRP laminate thickness of $t_{\mathrm{FRP}} = 0.5$ mm. Accordingly, Fig. 8(a) separately shows the curvature at rupture within the stiffener and FRP laminate against the elastomer modulus. Obviously, a compliant elastomer efficiently attracts the bending normal strain and also decouples the stiffener from the FRP laminate. In contrast, the FRP laminate is hardly effected by the elastomer modulus. The other investigated key parameter is the distance h_{in} of the stiffener to the FRP laminate. Figure 8(b) presents $\hat{\kappa}_x^{\mathrm{sti}}$ against h_{in} for three different elastomer moduli. Interestingly, the curvature at rupture rises for increasing distance h_{in}. The reason is

the stronger decoupling of stiffeners and FRP laminate which obviously dominates over the increasing bending normal strain.

5. Conclusions

This paper presents a new skin structure for curvature morphing applications. The concept, the corresponding manufacturing process, static bending experiments and first numerical investigations are presented. The suggested skin mainly features a similar morphing curvature at rupture as a corresponding FRP skin. However, the ratio of transverse to morphing bending modulus is in the range of $30 - 50$ (unidirectional GFRP exhibits $0.3 - 0.4$). Additionally, due to this advantageous stiffness ratio, this skin hardly shows any anticlastic bending deformations. Further investigations will focus on cyclic tests and the integration of an efficient de-icing system, lightning strike and abrasion protection.

Acknowledgement

This work has been funded by the German Science foundation (DFG) within the special research field 880 (SFB 880).

References

[1] S. Barbarino, O. Bilgen, R. M. Ajaj, M. I. Friswell, and D. J. Inman. A review of morphing aircraft. *J Intell Mater Syst Struct*, 22:823–877, 2011.

[2] M. Burnazzi and R. Radespiel. Design of a droopnose configuration for a coanda active flap application. *In: 51th AIAA Aerospace Sciences Meeting including the New Horizons Forum and Aerospace Exposition, Grapevine*, AIAA 2013-0487, 2013.

[3] M. Kintscher, M. Wiedemann, H. P. Monner, O. Heintze, and T. Kühn. Design of a smart leading edge device for low speed wind tunnel tests in the European project SADE. *Int J Struct Integ*, 2:383–405, 2011.

[4] A. Schmitz and P. Horst. Bending deformation limits for corrugated morphing skins. *In: 19th International Conference on Composite Materials, Montréal*, ICCM19:8942–8950, 2013.

[5] A. Schmitz and P. Horst. Bending deformation limits of corrugated unidirectionally reinforced composites. *Compos Struct*, 107:103–111, 2014.

[6] G. Tolf and P. Clarin. Comparison between flexural and tensile modulus of fibre composites. *Fibre Sci Technol*, 21:319–326, 1984.

[7] A. Schmitz and P. Horst. Numerical modelling of the change in stiffness properties of cross-ply laminates subjected to large bending curvatures. *Key Eng Mater*, 577-578:173–176, 2014.

[8] A. Schmitz and P. Horst. A finite element unit-cell method for homogenised mechanical properties of heterogeneous plates. *Compos Part A*, 61:23–32, 2014.